

Spatial and temporal distribution of γ H2AX fluorescence in human cell cultures following synchrotron-generated X-ray microbeams: lack of correlation between persistent γ H2AX foci and apoptosis

Danielle L. Anderson,^a Razmik Mirzayans,^{a,b} Bonnie Andrais,^b E. Albert Siegbahn,^c B. Gino Fallone^{a,d} and Brad Warkentin^{a,d*}

^aOncology, University of Alberta, 11560 University Avenue, Edmonton, AB T6G 1Z2, Canada,

^bExperimental Oncology, Cross Cancer Institute, 11560 University Avenue, Edmonton,

AB T6G 1Z2, Canada, ^cMedical Physics, Stockholm University, Box 260, S-17176 Stockholm,

Sweden, and ^dMedical Physics, Cross Cancer Institute, 11560 University Avenue, Edmonton,

AB T6G 1Z2, Canada. *E-mail: brad.warkentin@albertahealthservices.ca

Formation of γ H2AX foci (a marker of DNA double-strand breaks), rates of foci clearance and apoptosis were investigated in cultured normal human fibroblasts and p53 wild-type malignant glioma cells after exposure to high-dose synchrotron-generated microbeams. Doses up to 283 Gy were delivered using beam geometries that included a microbeam array (50 μm wide, 400 μm spacing), single microbeams (60–570 μm wide) and a broad beam (32 mm wide). The two cell types exhibited similar trends with respect to the initial formation and time-dependent clearance of γ H2AX foci after irradiation. High levels of γ H2AX foci persisted as late as 72 h post-irradiation in the majority of cells within cultures of both cell types. Levels of persistent foci after irradiation *via* the 570 μm microbeam or broad beam were higher when compared with those observed after exposure to the 60 μm microbeam or microbeam array. Despite persistence of γ H2AX foci, these irradiation conditions triggered apoptosis in only a small proportion (<5%) of cells within cultures of both cell types. These results contribute to the understanding of the fundamental biological consequences of high-dose microbeam irradiations, and implicate the importance of non-apoptotic responses such as p53-mediated growth arrest (premature senescence).

1. Introduction

Microbeam radiation therapy (MRT) employs synchrotron X-rays shaped into an array of quasi-parallel microbeams to treat solid tumours. MRT differs markedly from conventional therapies in three key aspects: (i) the dose distribution delivered to the tumours is spatially fractionated (microbeams are typically 25–100 μm wide and separated by 100–400 μm), (ii) extremely high doses (hundreds of Gy) are delivered in the microbeam paths in a single high-dose-rate (thousands of Gy s^{-1}) fraction, and (iii) the polyenergetic synchrotron X-rays are relatively low in energy (\sim 50–600 keV) (Slatkin *et al.*, 1992, 1995; Laissue *et al.*, 1998; Brauer-Krisch *et al.*, 2010). Animal studies have demonstrated that MRT can achieve similar or improved tumour control while resulting in reduced normal tissue toxicity when compared with single-fraction broad-beam irradiations (Laissue *et al.*, 1998, 2007; Dilmanian

et al., 2001, 2002, 2003; Miura *et al.*, 2006; Regnard *et al.*, 2008; Serduc *et al.*, 2008; Bräuer-Krisch *et al.*, 2010; Crosbie *et al.*, 2010). A better understanding of normal and tumour tissue response to high-dose microbeams would advance the present preclinical state of MRT, and may lead to translational advancements in conventional therapies.

The mechanisms underlying the biological responses to high-dose microbeams are complex and not yet fully understood. Animal studies have suggested that the differential responses between normal (skin) and cancerous (mammary) tissues might reflect differences at cellular levels in terms of DNA repair and apoptotic cell death (Crosbie *et al.*, 2010). The γ H2AX assay has been instrumental in measuring DNA damage after microbeam irradiation in various mammalian cell types both *in vitro* and *in vivo* (Kashino *et al.*, 2009; Crosbie *et al.*, 2010; Sprung *et al.*, 2011; Rothkamm *et al.*, 2012). Phosphorylation of the histone H2A variant H2AX on Ser139

is an important early event in the cellular response to ionizing radiation and other genotoxic agents that induce DNA double-strand breaks (DSBs) (Fernandez-Capetillo *et al.*, 2004). Hundreds of H2AX molecules in the chromatin surrounding a DSB are rapidly phosphorylated on this residue after irradiation, which can be visualized as a distinct nuclear focus by immunofluorescence microscopy (Pilch *et al.*, 2003). These phosphorylated H2AX (γ H2AX) foci are believed to serve as a platform for the recruitment of DNA repair and checkpoint signalling factors (Fernandez-Capetillo *et al.*, 2004), including p21 (Koike *et al.*, 2011). There is compelling evidence that DSBs provide the primary signal for H2AX phosphorylation (Fernandez-Capetillo *et al.*, 2004). Accordingly, the quantification of γ H2AX foci at relatively short times (*e.g.* 0.5 h) after irradiation has emerged as a widely used marker of DSBs that are detected by the cell (Pilch *et al.*, 2003; Fernandez-Capetillo *et al.*, 2004; Mirzayans *et al.*, 2006; Kuo & Yang, 2008; Wang *et al.*, 2011).

In the current study we report the responses triggered by high-dose synchrotron microbeam irradiations of varying geometry in cultured normal human fibroblasts and malignant glioma cells (hereafter NHFs and MGCs, respectively). The experiments were conducted on one of the Biomedical Imaging and Therapy (BMIT) beamlines at the Canadian Light Source located in Saskatoon (Saskatchewan, Canada). Our studies employed immunofluorescence assays that could be performed with methanol-fixed samples to facilitate processing and microscopic evaluation at our laboratory in Edmonton (Alberta, Canada). The γ H2AX immunofluorescence assay coupled with nuclear counterstaining with DAPI (4',6-diamidino-2-phenylindole) was used to measure DNA damage and morphological changes associated with apoptotic cell death (*i.e.* nuclear fragmentation) as a function of time after irradiation and beam geometry. Our results provide new insights into microbeam-triggered γ H2AX formation, rates of γ H2AX clearance, and lethality in cultured human cells.

2. Methods

2.1. Cells and culture conditions

The GM10 normal human fibroblast strain and the p53 wild-type A172 malignant glioma cell line were cultured as monolayers in DMEM/F12 medium supplemented with 10% (vol/vol) fetal bovine serum as described by Mirzayans *et al.* (2005). For experiments, cells were plated in 150 mm tissue culture dishes (2×10^6 cells/30 ml medium/dish) containing 25×75 mm sterile microscope slides, and then incubated for two days; under these conditions, cultures of both cell types reached 95–100% confluency prior to irradiation. The slides were placed in 50 ml tubes filled with fresh growth medium; the tubes were tightly sealed and then transported between the cell culture laboratory at the University of Saskatchewan and the Canadian Light Source (CLS), both located in Saskatoon (SK, Canada).

2.2. X-ray source and irradiation conditions

The CLS is a third-generation synchrotron facility that has a storage ring energy of 2.9 GeV and, presently, a maximum current of 250 mA. The samples were irradiated on the 05B1-1 beamline, which has a 1.354 T bending-magnet source. The beam was filtered by 0.934 mm Cu to produce a beam with a mean energy of 52 keV and a full width at half-maximum (FWHM) of 23.5 keV, as predicted by the *SPECTRA* software (Tanaka & Kitamura, 2001). The *SPECTRA* output was verified by comparing the percent depth dose (PDD) curve in water measured using a thimble ionization chamber (Wellhofer IC-10) with a Monte Carlo simulated PDD curve based on the *SPECTRA*-generated energy spectrum. An average difference of 0.5% was observed between the measurements and simulation over the 15 cm depth.

The cell samples, each on an individual microscope slide, were placed in a media-filled jig that ensured consistent placement of each sample during irradiation (Fig. 1). The medium in the jig was changed approximately every 8 h. The samples were positioned 26 m from the source, and 1 m from the multi-slit collimator (MSC). Samples were irradiated with doses of 1.4, 14, 71 or 283 Gy in the microbeam path. In addition, three conditions for the non-irradiated controls were investigated: samples that remained in the incubator until fixation; samples that were transported in tubes to the CLS and back to the incubator before fixation; and samples that were transported to the CLS and placed in the irradiation jig containing irradiated medium (but were not themselves exposed to X-rays) then subsequently transported back to the

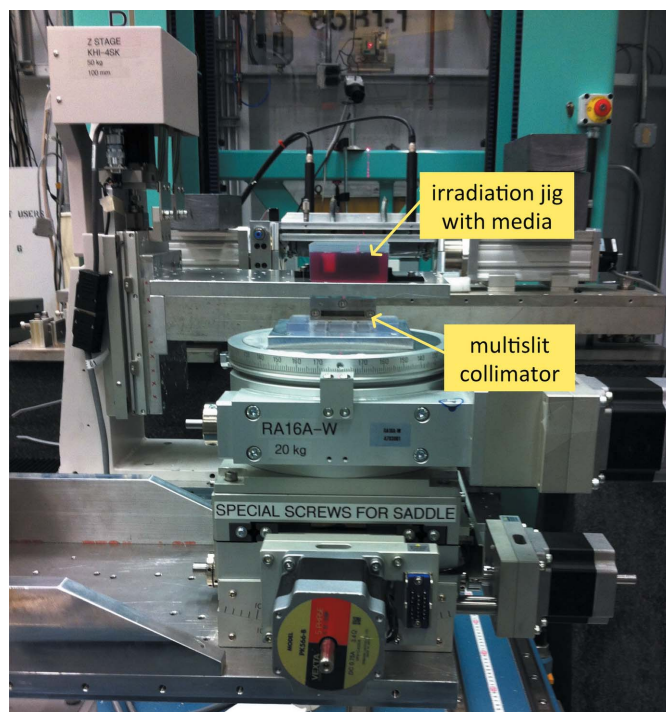


Figure 1 A beam's eye view of the experimental set-up showing the multi-slit collimator that produced the microbeam array and, 1 m downstream, the media-filled irradiation jig containing a sample. Using motorized stages, the collimator and jig are centred in the beam before irradiation.

incubator. Three beam geometries were considered: (i) an array of 75 microbeams with a centre-to-centre spacing of 400 μm , and each measuring 4 mm tall and 50 μm wide; (ii) single microbeams with a height of 4 mm and widths of 60, 100 or 570 μm ; and (iii) a broad beam that was 4 mm vertically and 32 mm horizontally. The microbeam array was created using the 8 mm-thick tungsten MSC (Usinage & Nouvelles Technologies, Moubier, France), while the single microbeams were created using vertical slits, and the broad beam shape was defined by the beamline jaws. Cells were incubated for periods of between 0.5 and 72 h post-irradiation to consider the time evolution of damage.

Following irradiation, for all but the earliest time point of 0.5 h, the samples were returned to their media-filled tubes and transported back to the cell culture laboratory for incubation for their prescribed incubation times. The 0.5 h samples were incubated in medium at room temperature without being returned to the incubator due to time restrictions. At the appropriate time following irradiation, samples were rinsed with phosphate-buffered saline (PBS) and fixed in methanol; slides were stored in 100% methanol at 253 K. Pilot experiments with ^{60}Co γ -irradiated cultures demonstrated that storing cells in methanol for several weeks post-irradiation does not influence the quality of γH2AX immunostaining.

2.3. γH2AX immunostaining and imaging

The γH2AX immunostaining procedure was carried out using well established techniques that have been published previously (Mirzayans *et al.*, 2006). The fixed cells (on microscope slides) were rinsed with PBS then incubated for 45 min with a blocking solution consisting of PBS containing 5% non-fat dry Carnation milk. Subsequently they were incubated with mouse anti- γH2AX antibody (anti-phosphohistone H2AX, Ser139, clone JBW301; Millipore, Billerica, MA, USA) for 1 h. The cells underwent 3×10 min washes with PBS containing 0.1% (vol/vol) Tween-20, followed by 60 min incubation with AlexaFluor 488 goat anti-mouse IgG (Life Technologies, Carlsbad, CA, USA). Antibodies were diluted (1:100 for γH2AX and 1:250 for AlexaFluor 488) in PBS containing 5% non-fat dry milk. Slides were incubated with 170 μL of each antibody on parafilm for 1 h at room temperature in a humidified dark environment. Following incubation with the AlexaFluor 488 antibody, the slides were washed for 2×10 min with PBS-Tween-20 and finally 1×10 min in PBS. DAPI counterstaining was performed to identify the location of the cells' nuclei and to visualize nuclear morphology. To this end, fixed cells on slides were overlaid with a mounting solution (90% glycerol in PBS) containing DAPI (50 $\mu\text{g ml}^{-1}$), covered with coverslips, and kept in the dark at 277 K.

Fluorescence microscopy of the immunostained samples was performed using a Zeiss Axioplan 2 microscope (Zeiss, Jena, Germany) in conjunction with an X-Cite 120 PC fluorescent lamp (EXFO, Quebec, QC, Canada) and suitable filters. A Photometrics CoolSnap HQ CCD camera (Photometrics, Tuscon, AZ, USA) and *Metamorph* software (version 7.7.7.0;

Molecular Devices Corporation, Sunnyvale, CA, USA) were used to capture the immunofluorescence images. Two sets of images were taken over any given region of interest: (i) a γH2AX image with a 450–490 nm band filter (100 or 600 ms exposure); and (ii) a DAPI image with a band filter of 350–400 nm (20–50 ms exposure). The resultant images have pixel sizes of either 0.64 $\mu\text{m} \times 0.64 \mu\text{m}$ or 0.32 $\mu\text{m} \times 0.32 \mu\text{m}$ achieved by using a 10 \times or 20 \times objective lens, respectively.

2.4. Image analysis

Images were analysed using in-house software developed in the MATLAB (MathWorks, Natick, MA, USA) programming environment. The code used both DAPI and γH2AX fluorescence images to map fluorescence intensity as a function of lateral position (orthogonal to the beam's propagation and to the vertical height of the microbeams). The DAPI images were used to create a binary mask of the DNA material in the image. The mask was applied to the γH2AX images to separate the fluorescence signal in the nuclei from the background signal outside the nuclei. The γH2AX fluorescence was integrated in the vertical direction over a portion of the microbeam's height (67 μm) and normalized by the amount of nuclear material in each of these vertical regions. This produced a profile that was fit to a Gaussian curve (O'Haver, 2012) to determine the mean intensity in the peak (within the microbeam path), the mean intensity in the valley (between two microbeams), the FWHM of both the peak region, and the area under the curve. In some γH2AX images at late times after irradiation, the peak and valley regions could not be identified automatically by the software. In these situations the peak and valleys were identified by manual inspection of the image; if still not distinguishable, the fluorescence intensities for both peak and valley regions were taken as the mean intensity of the image. We previously compared this automated method of analysing γH2AX -immunostained images with the conventional method of quantification through manual counting of γH2AX foci following radiation exposure (Anderson *et al.*, 2013). It was shown that the two methods yield similar trends, with the automated method providing increased speed, a higher dynamic range and improved objectivity. The automated method is, however, more prone to artefactual scoring of fluorescent intensity not originating from γH2AX foci [*e.g.* pan-stained nuclei exhibiting bright staining with no distinct foci (Marti *et al.*, 2006)]. In the current study, only the automated analysis (supplemented *via* manual inspection when necessary) was used to extract spatial patterns of γH2AX distributions from the large number of slides irradiated. Each datum point reported herein represents the mean and standard deviation of 15–50 measurements. In addition, high-resolution DAPI images were inspected manually to assess apoptotic morphology (*i.e.* nuclear condensation and/or fragmentation).

2.5. Monte Carlo and experimental dosimetry

The dose rate of the open synchrotron X-ray beam in air was determined using a Capintec PR06C ionization chamber

Table 1

Peak and valley doses delivered at a depth of 2 cm in water for the central microbeam of the microbeam array.

	Peak dose (Gy)	Valley dose (Gy)
Dose 1	1.4	0.02
Dose 2	14	0.2
Dose 3	71	1.1
Dose 4	283	4.3

to be $0.76 \text{ mGy mA}^{-1} \text{ s}^{-1}$. The Monte Carlo package *PENELOPE* (Salvat *et al.*, 2009) was used to estimate the decrease in dose rate when moving from the open beam to a $50 \text{ }\mu\text{m}$ -wide microbeam, and to simulate the dose distribution delivered by a microbeam array in a water phantom. The energy spectrum was calculated using the *SPECTRA* software (Tanaka & Kitamura, 2001) and the characteristics of the CLS storage ring and BMIT 05B1-1 beamline described in §2.2. Simulations were performed with a single $50 \text{ }\mu\text{m}$ -wide 4 mm -tall X-ray microbeam perpendicularly incident on a water phantom having dimensions of $10.7 \text{ cm} \times 4.8 \text{ cm} \times 12.9 \text{ cm}$, matching those of the medium-filled irradiation jig. The dose distribution was calculated using 10^8 histories, a spatial resolution in the depth direction of 1 mm , and a varying lateral resolution that was $1 \text{ }\mu\text{m}$ inside and close to the microbeam, and increased with distance from the microbeam. As done in several previous MRT Monte Carlos studies (Siegbahn *et al.*, 2006; Spiga *et al.*, 2007; Serduc *et al.*, 2010; Martínez-Rovira & Prezadoa, 2011), superposition of the single microbeam distribution was used to calculate the dose distribution of the full array, which contained 75 microbeams spaced by $400 \text{ }\mu\text{m}$ (centre-to-centre).

3. Results

3.1. Monte Carlo calculated dose distributions

The Monte Carlo simulated dose distribution is shown in Fig. 2 for the central three microbeams in the 75 microbeam array. Based on this simulation, the peak-to-valley dose ratio for the geometry considered ($50 \text{ }\mu\text{m}$ width, $400 \text{ }\mu\text{m}$ spacing) at a depth of 2 cm in water is 65 ± 1 . This depth was chosen to match the depth in the medium at which the cell culture samples were positioned during irradiations. The peak and valley doses delivered to the cell cultures are reported in Table 1.

3.2. Spatial and temporal distribution of γH2AX fluorescence in cell cultures following synchrotron X-ray irradiation

3.2.1. Immunofluorescence signal following irradiation by a synchrotron-generated microbeam array as a function of delivered dose. The presence of γH2AX immunofluorescence in cell cultures was visible at 0.5 h following exposure to the array of synchrotron microbeams for all doses delivered (1.4, 14, 71 and 283 Gy). Fluorescence microscopy images of MGCs and NHFs are shown in Fig. 3 for doses of 14, 71 and 283 Gy and different times (between 0.5 and 48 h) following irradiation.

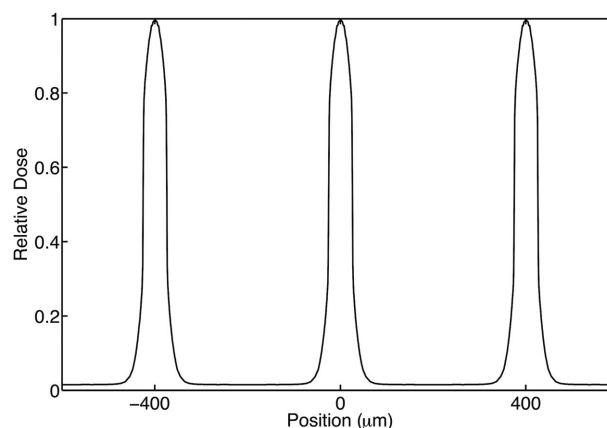


Figure 2

The Monte Carlo simulated relative dose distribution at a depth of 2 cm in water resulting from an array of $50 \text{ }\mu\text{m}$ -wide microbeams with centre-to-centre (ctc) spacing of $400 \text{ }\mu\text{m}$.

tion. We observed a non-linear increase in peak fluorescence intensity measured 0.5 h after irradiation as a function of delivered peak dose, as plotted in Fig. 4. The fluorescence intensity in the peak was measured as the central 25% of the FWHM of the curve. Fig. 4 also shows the valley fluorescence intensity as a function of dose, where the valley region was defined as the region measured two peak widths (FWHM) away from the peaks on either side of the valley of interest. The 0 Gy data point is the average of the fluorescence inten-

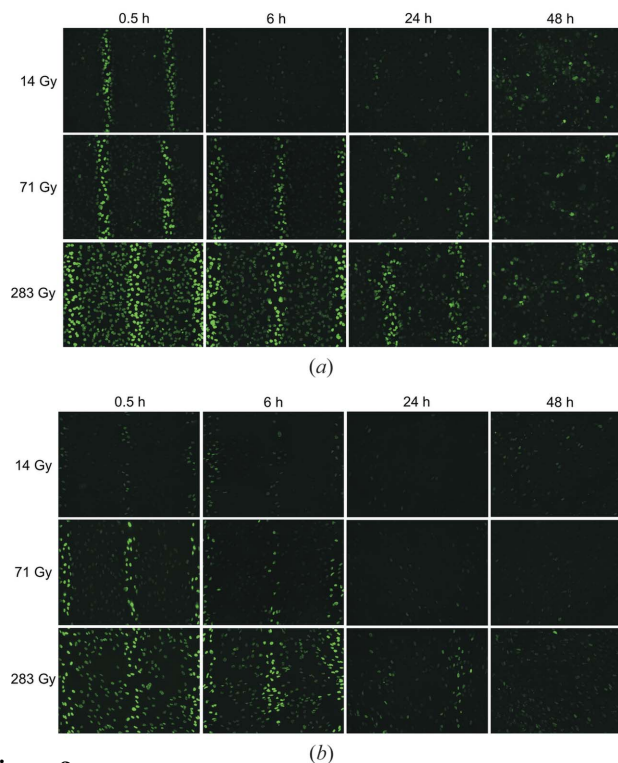


Figure 3

The γH2AX immunofluorescence in (a) MGCs and (b) NHFs following irradiation by the microbeam array ($50 \text{ }\mu\text{m}$ width, $400 \text{ }\mu\text{m}$ ctc). Samples are shown for doses of 14, 71 and 283 Gy, and times of 0.5, 6, 24 and 48 h after irradiation. Images were taken with a $10\times$ objective lens. The image dimensions are $666 \text{ }\mu\text{m}$ vertically \times $891 \text{ }\mu\text{m}$ horizontally.

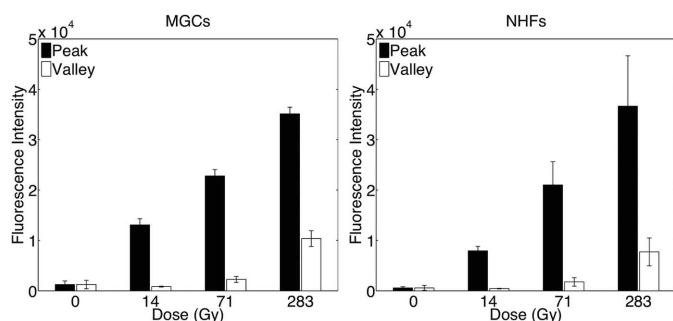


Figure 4
The γ H2AX immunofluorescence intensity in the peak and valley regions in MGCs (left) and NHFs (right) measured 0.5 h after irradiation with the microbeam array as a function of dose delivered in the peak.

sity in samples from all three control conditions (described in §2.2), as there was no significant difference in fluorescence intensity for the three conditions.

The widths of the peak regions were measured at 0.5 h *via* the peak-fitting algorithm in both cell types. In NHFs, the peak width was $55.2 \pm 5.1 \mu\text{m}$, and in MGCs the width was $56.6 \pm 9.3 \mu\text{m}$. The ten central peak widths measured at the surface of the irradiation jig [using GafChromic HD810 film (ISP Technologies, NJ, USA)] and at 2 cm depth in media (using GafChromic EBT2 film) were 55.8 ± 2.6 and $57.9 \pm 0.9 \mu\text{m}$, respectively.

3.2.2. Change in immunofluorescence signal with time after irradiation with a synchrotron-generated microbeam array. Fig. 3 illustrates the decrease in γ H2AX immunofluorescence in both cell types at times of 6, 24 and 48 h after irradiation, as compared with the initial fluorescence measured at 0.5 h. The γ H2AX fluorescence intensities in both the peak and valley regions at times up to 24 h following a peak dose of 283 Gy are plotted in Fig. 5. In general, the γ H2AX fluorescence intensity decreases in a similar manner in both cell types. The peak fluorescence decreases most rapidly between 0.5 and 12 h after irradiation, and only minimal changes occur between 12 and 24 h. The valley fluorescence remains relatively constant for the first 6 h, decreases most significantly between 6 and 9 h, then remains relatively constant again until 24 h. The most conspicuous difference in γ H2AX fluorescence clearance between MGCs

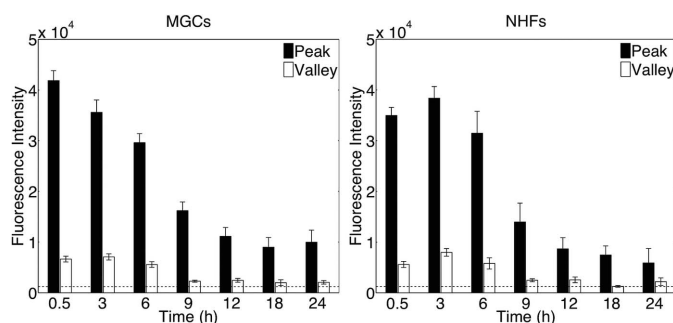


Figure 5
The γ H2AX immunofluorescence intensity in the peak and valley regions in MGCs (left) and NHFs (right) measured between 0.5 and 24 h after a 283 Gy irradiation with the microbeam array. The dashed line indicates the mean fluorescence intensity in controls.

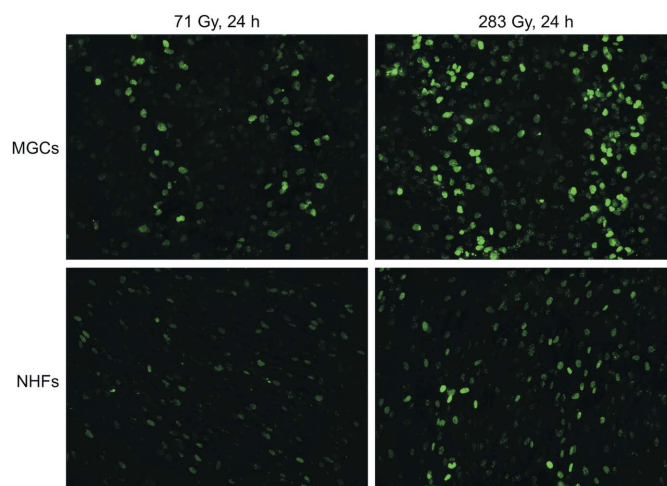


Figure 6
 γ H2AX immunofluorescence in MGCs (top) and NHFs (bottom) at 24 h after a 71 Gy (left) and a 283 Gy (right) irradiation with the microbeam array illustrates the prolonged persistence of peak and valley regions in MGCs compared with NHFs.

and NHFs is apparent at 24 h. For a 283 Gy irradiation, the peak and valley structure remains prominent in MGCs up to 24 h, while the fluorescence in these two regions at 24 h in NHFs is either much more similar or even indistinguishable for some samples. The greater difference between peak and valley fluorescence intensity at 24 h evident in MGC samples is readily apparent in the γ H2AX images for 71 and 283 Gy doses shown in Fig. 6. The time dependence of the cell culture response to lower doses was sampled at a coarser temporal resolution; nevertheless, there appeared to be a similar rate of fluorescence loss between 0.5 and 6 h, and a less defined peak and valley structure at 24 h compared with the 283 Gy samples. At 48 h (data not shown) and 72 h (Fig. 7), there are persistent (above background) γ H2AX foci visible in the

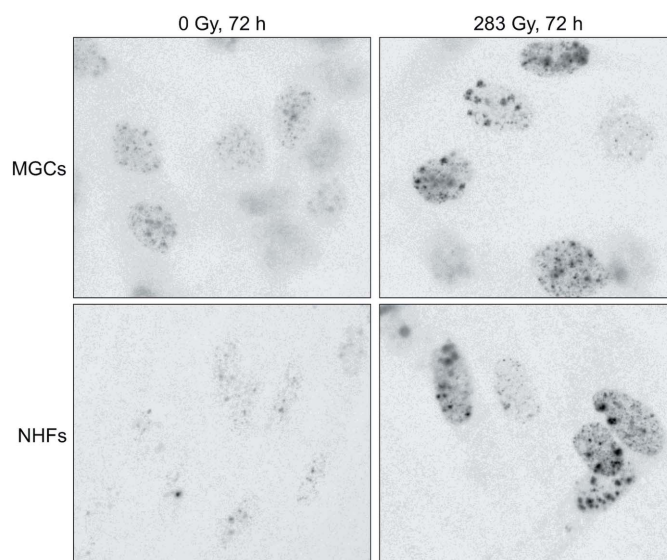


Figure 7
 γ H2AX images at 72 h in control (left) and 283 Gy-irradiated (right) MGCs (top) and NHFs (bottom) show the persistence of γ H2AX fluorescence signal in irradiated samples at long times post-irradiation.

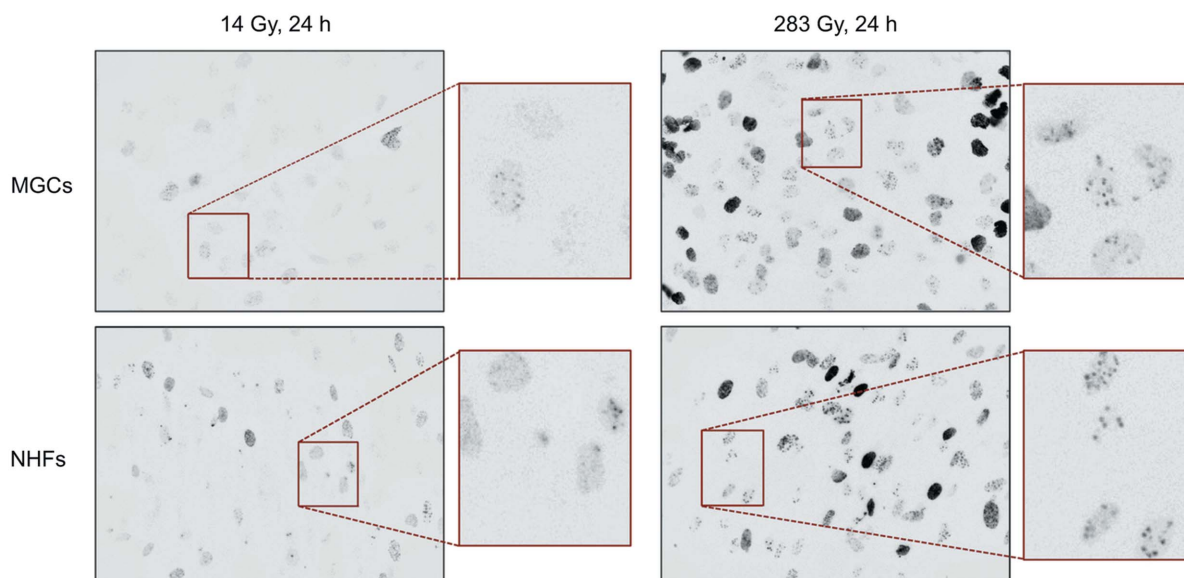


Figure 8
 The γ H2AX immunofluorescence intensity in MGCs (top) and NHFs (bottom) at 24 h after irradiation with the microbeam array. The samples on the left were irradiated with a 14 Gy peak dose and corresponding 0.2 Gy valley dose, while the samples on the right received a 283 Gy peak and 4.3 Gy valley dose. The image dimensions are 333 μ m vertically \times 445 μ m horizontally.

irradiated samples of both cell types. However, at these late times the microbeam pattern is no longer discernible, as the foci are not clustered in distinct peak and valley regions.

A more detailed examination of the foci present in the valley regions of the cell cultures at 24 h revealed a slower clearance of γ H2AX signal than expected based on the valley dose, and the observed clearance in the peak regions. Fig. 8 shows the results for both cell types at 24 h following peak/valley doses of either 14/0.2 Gy (left) or 283/4.3 Gy (right) delivered *via* the microbeam array. The MGC-283 Gy image is centred on the valley region (the microbeam paths are along the left and right edges of the image), while the three other images show a mixed zone because the peaks and valleys are indistinguishable in these images. We observed more clearance in directly irradiated cells receiving 14 Gy than in cells receiving only 4.3 Gy in the valley, but surrounded by 283 Gy peak regions.

3.2.3. Change in immunofluorescence signal with beam width after irradiation with a synchrotron-generated microbeam array, single microbeams and a broad beam.

During two experimental sessions at the CLS, the influence of beam size on fluorescence clearance was investigated by comparing samples irradiated using the microbeam array, a single microbeam and a broad beam. Experiment 1 included the 50 μ m microbeam from the full array (labelled MSC), and three single microbeams (widths of 60, 100 and 570 μ m), all 4 mm tall. Experiment 2 included another 50 μ m microbeam from the full array (labelled MSC2) and the response to the 4 mm \times 32 mm broad beam (labelled BB). Images of the γ H2AX-immunostained nuclei for both cell types are shown in Fig. 9 at 24 h after a 71 Gy irradiation. Compared with the microbeam from the full array (MSC), we observed similar γ H2AX fluorescence remaining at 24 h with the 60 μ m-wide single microbeam, and more fluorescence remaining following

exposure to the 570 μ m-wide microbeam. Considering the data from experiment 2, we observed less clearance following a broad beam irradiation compared with the microbeam array (MSC2). In general, the nuclei in the wide microbeam (570 μ m) or broad beam images contain, on average, a greater number of remaining foci at 24 h compared with the narrow microbeam (50 or 60 μ m) images. The residual foci following exposure to the 100 μ m microbeam had mixed results. In NHFs, the number of residual γ H2AX foci was higher than for the 60 μ m-wide microbeam and more similar to the 570 μ m-wide microbeam. The opposite was true for MGCs, *i.e.* the response of these cells to the 100 μ m microbeam was very similar to the 60 μ m microbeam and had fewer remaining foci than the 570 μ m microbeam. Differences between the narrow microbeams (50 or 60 μ m) compared with the wide microbeam (570 μ m) or the broad beam at 24 h were more obvious for NHFs than MGCs. It is possible, however, that this may just reflect the slightly different rates of γ H2AX clearance between the two cell types, as was described in §3.2.2.

3.3. Cellular morphology examined to identify apoptotic cells

To investigate cellular fates following high-dose irradiations, cells with apoptotic morphology (see, for example, the inset in Fig. 10) were counted in all microbeam-irradiated samples for times up to 72 h after irradiation, and in broad-beam-irradiated samples for times up to 24 h. Since microbeam peaks and valleys are indistinguishable for late time points, for all microbeam samples the apoptotic cells were counted within the entire microbeam array path encompassing both peaks and valleys. Apoptotic cells were identified by morphology (*i.e.* nuclear fragmentation and/or condensation). The incidence of apoptotic cells is shown in Fig. 10 where both subplots have the same scale for comparison between cell

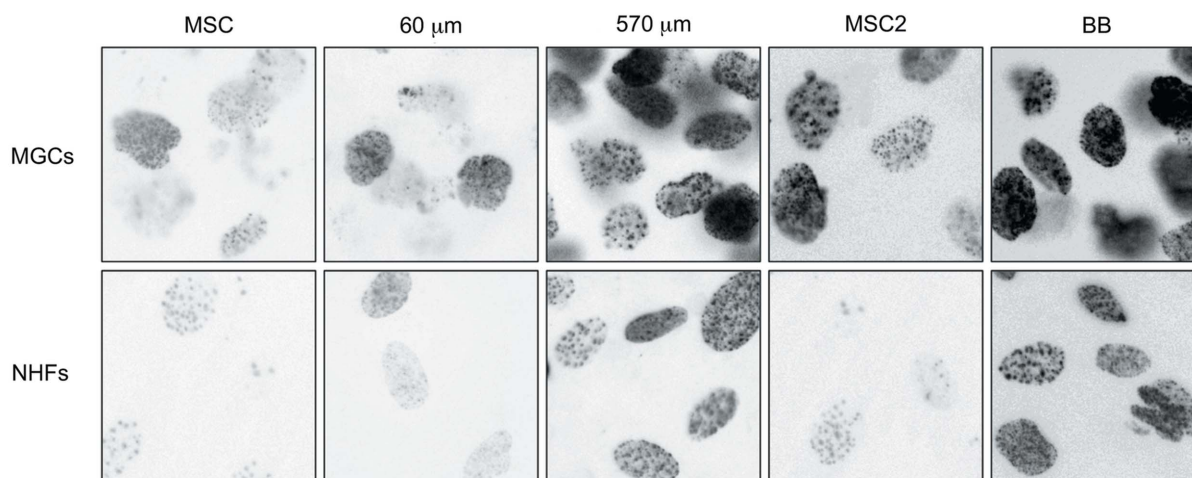


Figure 9
 Images of MGCs (top) and NHFs (bottom) 24 h after a 71 Gy dose. The first three columns of images were acquired during a first experimental session at the CLS, and correspond to cells irradiated with the microbeam array (MSC), or single microbeams of either 60 or 570 μm width. Images from a second session at the CLS (the last two columns of images) include irradiation using a microbeam array (MSC2) or a broad beam (BB). Images were taken within the peak region (if apparent).

types. Even at the high doses considered, very few apoptotic cells were present. For MGCs, the maximum occurrence of apoptotic cells for any time and dose combination following microbeam (MB) irradiation was $0.17 \pm 0.03\%$ (283 Gy, 72 h) and $0.20 \pm 0.04\%$ (283 Gy, 24 h) following broad beam (BB) exposure. In response to the microbeam array, there was a significant difference between the proportion of apoptotic cells at 72 h *versus* any other time points. There was also an increase in the number of apoptotic cells at 24 h following broad beam irradiation *versus* the microbeam-irradiated cells at 24 h for 71 and 283 Gy. Overall, however, MGCs showed an

extremely high resistance to undergoing apoptosis following doses up to several hundred Gy.

The percentage of apoptosis in microbeam-irradiated NHFs was slightly higher than was found for MGCs, but still extremely low, with a maximum incidence of $0.75 \pm 0.19\%$ at 72 h after a 283 Gy dose of irradiation. At any time point, the number of apoptotic cells was highest following the largest dose (283 Gy), and for any dose the most apoptotic cells were found at 72 h after irradiation. There was an increase in the amount of apoptotic NHFs present at 24 h in broad-beam-irradiated samples compared with the amount of apoptotic cells present following microbeam irradiations of equivalent doses. After a broad beam dose of 283 Gy, there were $2.7 \pm 0.5\%$ apoptotic cells. Despite the higher prevalence of apoptosis in NHFs, particularly for broad beam irradiations, the overall rate of apoptosis is extremely low ($<5\%$). Thus, apoptosis is not the preferred response of these cultures to ionizing-radiation-induced DNA damage under the conditions we investigated.

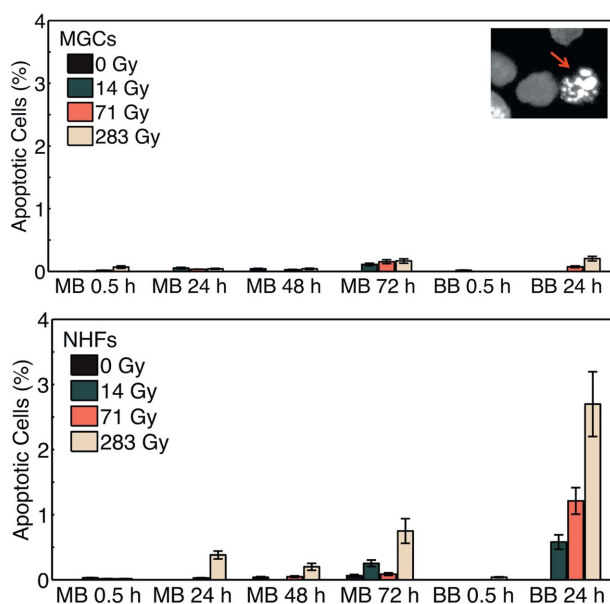


Figure 10
 The incidence of apoptotic nuclei after irradiation with the microbeam array (labelled MB) or the 4 mm \times 32 mm broad beam (labelled BB) at various times after exposure (0.5–72 h) and various doses (0–283 Gy) for MGCs and NHFs. An example of an apoptotic cell is indicated by the arrow.

4. Discussion

The Biomedical Imaging and Therapy (BMIT) beamlines at the CLS offer novel techniques using synchrotron X-rays in both imaging and therapy, including the development of an MRT program. Our experiments were performed using the 05B1-1 X-ray beamline at the CLS, the only fully commissioned BMIT beamline at the time of the experiments. Although this beamline provides a lower mean energy (52 keV) and considerably lower dose rate ($\sim 1.5 \text{ Gy s}^{-1}$) than typically used in MRT, the minimally divergent ($\sim 4 \text{ mrad}$) beam is able to provide the highly spatially fractionated dose distribution that is central to MRT's unique biological properties. The cellular response to high-dose synchrotron X-rays of several geometries was assessed using the γH2AX immunohistochemical assay in conjunction with the examination of

apoptotic cell morphology at several time points after irradiation.

To evaluate γ H2AX fluorescence, which was used as a surrogate for DNA damage, we employed an automated analysis that tallied fluorescence intensity from the immunostained cell cultures. Total fluorescence intensity was measured, in contrast to the more traditional method of counting individual γ H2AX foci, for two major reasons: (i) at these high doses the individual γ H2AX foci in the peak regions are too numerous to discern; and (ii) the automated analysis provides a time-efficient method of analysing the large number of samples that were treated. Using this assay we were able to visually identify peak and valley regions of irradiated samples, and quantify the γ H2AX fluorescence in a spatially dependent manner in each of these zones in cell cultures. We observed a non-linear increase in γ H2AX fluorescence intensity with increasing dose for a range of peak doses between 0 and 283 Gy. The sensitivity of the emitted γ H2AX fluorescence with respect to changing dose decreases with increasing dose, most likely due to overlapping individual foci at higher doses. Despite its benefits, this method of analysis does have some limitations. At low valley doses (below approximately 1 Gy), the automated analysis had insufficient sensitivity to separate the low number of high-intensity γ H2AX foci arising spontaneously or induced by ionizing radiation. In the low-dose valley region it is possible to overcome this issue by manually counting distinct γ H2AX foci. It becomes very difficult, however, to distinguish individual γ H2AX foci at doses of 14 Gy and above in the peak regions at 0.5 h after irradiation. Despite these challenges, our results show that the distribution of γ H2AX fluorescence following irradiation faithfully represents the delivered dose distribution, as shown by the agreement within error between the microbeam widths measured *via* radiochromic film and from the 0.5 h γ H2AX images. This supports the suggestion by Rothkamm *et al.* (2012) that γ H2AX immunostaining could be used for biological dose mapping in cell culture and in tissue sections. Even at the high doses typical of MRT, where counting foci to estimate the delivered dose is difficult, this assay could prove useful for verifying difficult irradiation geometries, such as interlaced microbeam arrays (*e.g.* Serduc *et al.*, 2010) in animal models at early times after irradiation, and perhaps inform the extent of DNA damage, beyond simply the delivered dose distributions, at late times following microbeam irradiations.

Although limitations of the assay exist, we were able to extract several interesting relationships between the distribution of γ H2AX immunofluorescence in cell culture at various times after microbeam irradiations with different doses and geometries. First, in response to the microbeam array, the two cell types had similar overall trends in terms of initial formation of γ H2AX foci and their rate of clearance. Specifically, the highest fluorescence signal occurred in the first 0.5–3 h in both cell types, and the signal intensity decreased with time. The most significant reduction in valley fluorescence was observed between 6 and 9 h. Although the overall trend of γ H2AX fluorescence clearance was very

similar for the two cell types, we observed that the rate of clearance in MGCs was slightly slower than in NHFs. At 24 h after irradiation, the peak and valley regions were still easily discernible in MGCs after a dose of 283 Gy, but not in NHFs. This effect was reflected in the constantly widening widths of the peak regions in NHFs with time, while the width in MGCs expanded more slowly. By 48 h after irradiation, the peak and valley regions were completely missing in both cell types. Although the microbeam pattern was lost according to the automated analysis, high-resolution images revealed the persistence of γ H2AX foci in both cell types at late times (up to 72 h) following irradiation.

We also observed an interesting effect in the valley clearance at 24 h after exposure. In a valley region exposed to only 4.3 Gy (corresponding to a peak dose of 283 Gy) we observed less clearance by 24 h than we observed in the mixed peak/valley regions that were exposed to a peak and valley dose of 14 and 0.2 Gy and incubation for 24 h, respectively. This suggests that the DNA damage response of the cells in the valley region is influenced by the heavily irradiated cells in the peak region. Whether this observation reflects intercellular communication (between cells within peak and valley regions) and/or cell movement (from peak to valley regions) remains to be determined. Additional investigations of this phenomenon are warranted to further the understanding of MRT's potential therapeutic benefit.

The response of MGCs and NHFs to X-ray beams of varying widths was investigated using the full microbeam array, three single microbeams and one rectangular broad beam. We observed more γ H2AX clearance for narrower microbeams (the 50 μ m-wide microbeam from the full array, and the 60 μ m single microbeam) than for the wider microbeam (570 μ m) and the broad beam. This difference in response with width was more easily visualized in NHFs. We suspect that this results from the slightly slower rate of γ H2AX clearance for MGCs discussed above, and not that the overall γ H2AX clearance following microbeam irradiation is necessarily better for NHFs over MGCs.

A straightforward interpretation of the γ H2AX clearance data is that DSBs induced under these conditions might be rejoined at a faster rate in NHFs than MGCs. However, alternative explanations cannot be ruled out given that radiation-triggered genomic abnormalities other than DSBs are also known to give rise to Ser139-H2AX phosphorylation and formation of γ H2AX-associated nuclear foci. Suzuki *et al.* (2006), for example, demonstrated that γ H2AX foci persist at times after irradiation when all detectable DSBs are rejoined, and concluded that the residual (persistent) foci indicate an aberrant chromatin structure, but not a DSB itself. In light of this, the only definitive conclusions that can be drawn from our observations are that genomic alterations that give rise to γ H2AX foci are induced in these cultures; that such alterations persist for the duration of the experiments (up to 72 h) after synchrotron microbeam irradiation; and that at late times after radiation exposure these foci are distributed uniformly, as opposed to being predominantly present in the peak region as was seen at early times post-irradiation.

The A172 MGCs used in the current study respond to ionizing radiation similarly to NHFs in terms of clonogenic survival (Mirzayans *et al.*, 2005) and activation of the p53 tumour suppressor (Mirzayans *et al.*, 2005, 2012), a key regulator of the DNA surveillance network (Mirzayans *et al.*, 2013). Although these cultures exhibit apoptosis resistance in response to moderate doses of ionizing radiation (*e.g.* 10 Gy) (Mirzayans *et al.*, 2012), we considered the possibility that the residual γ H2AX foci observed at late times after high-dose (*e.g.* 283 Gy) irradiation might reflect cells undergoing apoptosis. However, using morphological criteria (*i.e.* nuclear fragmentation and/or shrinkage), we observed very low frequency (<5%) of apoptotic cells in cultures of both cell types following high-dose synchrotron-generated X-ray microbeam irradiations. We observed a slightly elevated frequency of apoptosis in NHFs following broad beam irradiation at 2.7%, but MGCs remained below 0.5%. Further study would be useful to determine whether the high-dose microbeam conditions alter the frequency of apoptosis for other cell types for which apoptosis has been established as a significant damage response pathway at low to moderate doses.

For the cell types investigated in this work, one hypothesis is that the apoptosis-resistant phenotype of these cultures might be associated with p53-mediated upregulation of p21, a well characterized anti-apoptotic protein that acts at different levels of the death cascade (Mirzayans *et al.*, 2013; Gartel & Tyner, 2002) and engages the stress-induced premature senescence (SIPS) response (Mirzayans *et al.*, 2013). Cells that undergo the SIPS response enter a prolonged state of growth-arrest in which DNA replication ceases, but the cells remain viable and continue to secrete growth- and tumour-promoting factors (Mirzayans *et al.*, 2013). The preference of p53 wild-type human cells for SIPS as opposed to undergoing apoptosis has been previously demonstrated in response to conventional broad beam irradiation (Mirzayans *et al.*, 2005, 2010, 2012). The residual γ H2AX fluorescence observed at late times in this study may be an indicator of cells undergoing SIPS, since this response is also associated with high numbers of γ H2AX foci, presumably reflecting genomic instability (Mirzayans *et al.*, 2010).

The techniques reported here will facilitate the evaluation of DNA damage response to microbeam irradiation in different types of cultured human cells (*e.g.* normal *versus* cancerous) with different genetic background (*e.g.* TP53 status). Our results give credence to previous work (Kashino *et al.*, 2009; Crosbie *et al.*, 2010; Sprung *et al.*, 2011; Rothkamm *et al.*, 2012) suggesting that the γ H2AX immunofluorescence assay might be used as a reliable biological probe for evaluating DSBs at relatively short times (0.5 h) after synchrotron exposure. We have demonstrated that synchrotron exposure of p53 wild-type human cell cultures (normal fibroblasts and A172 MGCs) results in a high frequency of genomic instability, which is manifested as γ H2AX-associated nuclear foci that persist for long times (*e.g.* 72 h) post-irradiation but are not associated with apoptosis. Our studies motivate further *in vitro* and *in vivo* investigations on microbeam-triggered

early responses (*e.g.* DNA repair; cell cycle checkpoints) and late responses (*e.g.* apoptosis; SIPS) in human cells with differing p53 status.

Support for this work was provided by Vanier Canada Graduate Scholarships and Alberta Innovates – Health Solutions. The authors would like to thank Dr Rajni Chibbar and Ms Heather Neufeld for arranging the use of the GEMS cell culture laboratory at the University of Saskatchewan, as well as the BMIT beamline staff for their tireless support.

References

- Anderson, D., Andrais, B., Mirzayans, R., Siegbahn, E. A., Fallone, B. G. & Warkentin, B. (2013). *J. Instrum.* **8**, C06008.
- Bräuer-Krisch, E., Serduc, R., Siegbahn, E. A., Le Duc, G., Prezado, Y., Bravin, A., Blattmann, H. & Laissue, J. A. (2010). *Mutat. Res.* **704**, 160–166.
- Crosbie, J. C., Anderson, R. L., Rothkamm, K., Restall, C. M., Cann, L., Ruwanpura, S., Meachem, S., Yagi, N., Svalbe, I., Lewis, R. A., Williams, B. R. & Rogers, P. A. W. (2010). *Int. J. Radiat. Oncol. Biol. Phys.* **77**, 886–894.
- Dilmanian, F. A., Button, T. M., Le Duc, G., Zhong, N., Pena, L. A., Smith, J. A. L., Martinez, S. R., Bacarian, T., Tammam, J., Ren, B., Farmer, P. M., Kalef-Ezra, J., Micca, P. L., Nawrocky, M. M., Niederer, J. A., Recksiek, F. P., Fuchs, A. & Rosen, E. M. (2002). *Neuro-Oncol.* **4**, 26–38.
- Dilmanian, F. A., Morris, G. M., Le Duc, G., Huang, X., Ren, B., Bacarian, T., Allen, J. C., Kalef-Ezra, J., Orion, I., Rosen, E. M., Sandhu, T., Sathé, P., Wu, X. Y., Zhong, Z. & Shivaprasad, H. L. (2001). *Cell. Mol. Biol.* **47**, 485–493.
- Dilmanian, F. A., Morris, G. M., Zhong, N., Bacarian, T., Hainfeld, J. F., Kalef-Ezra, J., Brewington, L. J., Tammam, J. & Rosen, E. M. (2003). *Radiat. Res.* **159**, 632–641.
- Fernandez-Capetillo, O., Lee, A., Nussenzweig, M. & Nussenzweig, A. (2004). *DNA Repair*, **3**, 959–967.
- Gartel, A. L. & Tyner, A. L. (2002). *Mol. Cancer Ther.* **1**, 639–649.
- Kashino, G., Kondoh, T., Nariyama, N., Umetani, K., Ohigashi, T., Shinohara, K., Kurihara, A., Fukumoto, M., Tanaka, H., Maruhashi, A., Suzuki, M., Kinashi, Y., Liu, Y., Masunaga, S., Watanabe, M. & Ono, K. (2009). *Int. J. Radiat. Oncol. Biol. Phys.* **74**, 229–236.
- Koike, M., Yutoku, Y. & Koike, A. (2011). *Biochem. Biophys. Res. Commun.* **412**, 39–43.
- Kuo, L. J. & Yang, L. X. (2008). *In Vivo*, **22**, 305–309.
- Laissue, J. A., Blattmann, H., Wagner, H. P., Grotzer, M. A. & Slatkin, D. N. (2007). *Dev. Med. Child Neurol.* **49**, 577–581.
- Laissue, J. A., Geiser, G., Spanne, P. O., Dilmanian, F. A., Gebbers, J. O., Geiser, M., Wu, X. Y., Makar, M. S., Micca, P. L., Nawrocky, M. M., Joel, D. D. & Slatkin, D. N. (1998). *Int. J. Cancer*, **78**, 654–660.
- Marti, T. M., Hefner, E., Feeney, L., Natale, V. & Cleaver, J. E. (2006). *Proc. Natl Acad. Sci. USA*, **103**, 9891–9896.
- Martínez-Rovira, I. & Prezado, Y. (2011). *Med. Phys.* **38**, 4430–4439.
- Mirzayans, R., Andrais, B., Scott, A. & Murray, D. (2012). *J. Biomed. Biotechnol.* **2012**, 170325.
- Mirzayans, R., Andrais, B., Scott, A., Paterson, M. C. & Murray, D. (2010). *J. Cell. Physiol.* **223**, 57–67.
- Mirzayans, R., Andrais, B., Scott, A., Wang, Y. W. & Murray, D. (2013). *Int. J. Mol. Sci.* **14**, 22409–22435.
- Mirzayans, R., Scott, A., Cameron, M. & Murray, D. (2005). *Radiat. Res.* **163**, 53–62.
- Mirzayans, R., Severin, D. & Murray, D. (2006). *Int. J. Radiat. Oncol. Biol. Phys.* **66**, 1498–1505.

- Miura, M., Blattmann, H., Bräuer-Krisch, E., Bravin, A., Hanson, A. L., Nawrocky, M. M., Micca, P. L., Slatkin, D. N. & Laissue, J. A. (2006). *Br. J. Radiol.* **79**, 71–75.
- O'Haver, T. C. (May 2012). *Peak Fitter*, version 2.4, <http://terpconnect.umd.edu/~toh/spectrum/InteractivePeakFitter.htm>.
- Pilch, D. R., Sedelnikova, O. A., Redon, C., Celeste, A., Nussenzweig, A. & Bonner, W. M. (2003). *Biochem. Cell Biol.* **81**, 123–129.
- Regnard, P., Le Duc, G., Bräuer-Krisch, E., Troprès, I., Siegbahn, E. A., Kusak, A., Clair, C., Bernard, H., Dallery, D., Laissue, J. A. & Bravin, A. (2008). *Phys. Med. Biol.* **53**, 861–878.
- Rothkamm, K., Crosbie, J. C., Daley, F., Bourne, S., Barber, P. R., Vojnovic, B., Cann, L. & Rogers, P. A. W. (2012). *PLoS One*, **7**, e29853.
- Salvat, F., Fernandez-Varea, J. M. & Sempau, J. (2009). *PENELOPE, A Code System for Monte Carlo Simulation of Electron and Photon Transport*. OECD NEA, Issy-les-Moulineaux, France.
- Serduc, R., Bräuer-Krisch, E., Siegbahn, E. A., Bouchet, A., Pouyatos, B., Carron, R., Pannetier, N., Renaud, L., Berruyer, G., Nemoz, C., Brochard, T., Rémy, C., Barbier, E. L., Bravin, A., Le Duc, G., Depaulis, A., Estève, F. & Laissue, J. A. (2010). *PLoS ONE*, **5**, e9028.
- Serduc, R., van de Looij, Y., Francony, G., Verdonck, O., van der Sanden, B., Laissue, J., Farion, R., Bräuer-Krisch, E., Siegbahn, E. A., Bravin, A., Prezado, Y., Segebarth, C., Rémy, C. & Lahrech, H. (2008). *Phys. Med. Biol.* **53**, 1153–1166.
- Siegbahn, E. A., Stepanek, J., Bräuer-Krisch, E. & Bravin, A. (2006). *Med. Phys.* **33**, 3248–3259.
- Slatkin, D. N., Spanne, P., Dilmanian, F. A., Gebbers, J. O. & Laissue, J. A. (1995). *Proc. Natl Acad. Sci. USA*, **92**, 8783–8787.
- Slatkin, D. N., Spanne, P., Dilmanian, F. A. & Sandborg, M. (1992). *Med. Phys.* **19**, 1395–1400.
- Spiga, J., Siegbahn, E. A., Bräuer-Krisch, E., Randaccio, P. & Bravin, A. (2007). *Med. Phys.* **34**, 4322–4330.
- Sprung, C. N., Cholewa, M., Usami, N., Kobayashi, K. & Crosbie, J. C. (2011). *J. Synchrotron Rad.* **18**, 630–636.
- Suzuki, M., Suzuki, K., Kodama, S. & Watanabe, M. (2006). *Radiat. Res.* **165**, 269–276.
- Tanaka, T. & Kitamura, H. (2001). *J. Synchrotron Rad.* **8**, 1221–1228.
- Wang, M., Morsbach, F., Sander, D., Gheorghiu, L., Nanda, A., Benes, C., Kriegs, M., Krause, M., Dikomey, E., Baumann, M., Dahm-Daphi, J., Settleman, J. & Willers, H. (2011). *Cancer Res.* **71**, 6261–6269.